Antiferroelectricity in BiFeO$_3$ Ultrathin Films

Menghui Xia,[1] Sukriti Mantri,[2, *] L. Bellaiche,[2, 3] and Bin Xu[1, †]

[1]*Jiangsu Key Laboratory of Frontier Material Physics and Devices,*

School of Physical Science and Technology,

Soochow University, Suzhou 215006, China

[2]*Smart Ferroic Materials Center, Physics Department*

and Institute for Nanoscience and Engineering,

University of Arkansas, Fayetteville, Arkansas 72701, USA

[3]*Department of Materials Science and Engineering,*

Tel Aviv University, Ramat Aviv, Tel Aviv 6997801, Israel

This Supplemental Material includes:

- Section S1. Ferroelectric vs. antiferroelectric materials

- Section S2. Computational details

- Section S3. Bulk vs. film structures

- Section S4. Electrostatic model to explain the polarization in the O-like phase

- Section S5. Simple model to explain the FE-to-AFE size effect

- Section S6. P-E loops with various screening and temperature conditions

- Section S7. Strain and surface screening effects on thermal stability

SECTION 1. FERROELECTRIC VS. ANTIFERROELECTRIC MATERIALS

Both the ferroelectric (FE) and antiferroelectric (AFE) materials involve microscopic dipoles, but they differ in how those dipoles order and respond to an external electric field. In a FE, each unit cell has a net dipole that breaks the global inversion symmetry. The microscopic dipoles align parallel to each other, giving rise to a nonzero spontaneous macroscopic polarization. The polarization can be reversed by an applied electric field and form a single P-E hysteresis loop [see schematic illustration in Fig. S1(a)]. In contrast, an AFE unit cell is centrosymmetric and involves dipoles of opposite orientations, which produces a superstructure (two sublattices or modulated pattern) with "*ideally*" zero net polarization. To qualify as an AFE, the antiferroelectric ground state must be switchable to a field-induced polar (FE-like) state under a sufficiently high electric field, characterized by a double hysteresis loop formed under bipolar fields [see schematic illustration in Fig. S1(b)].
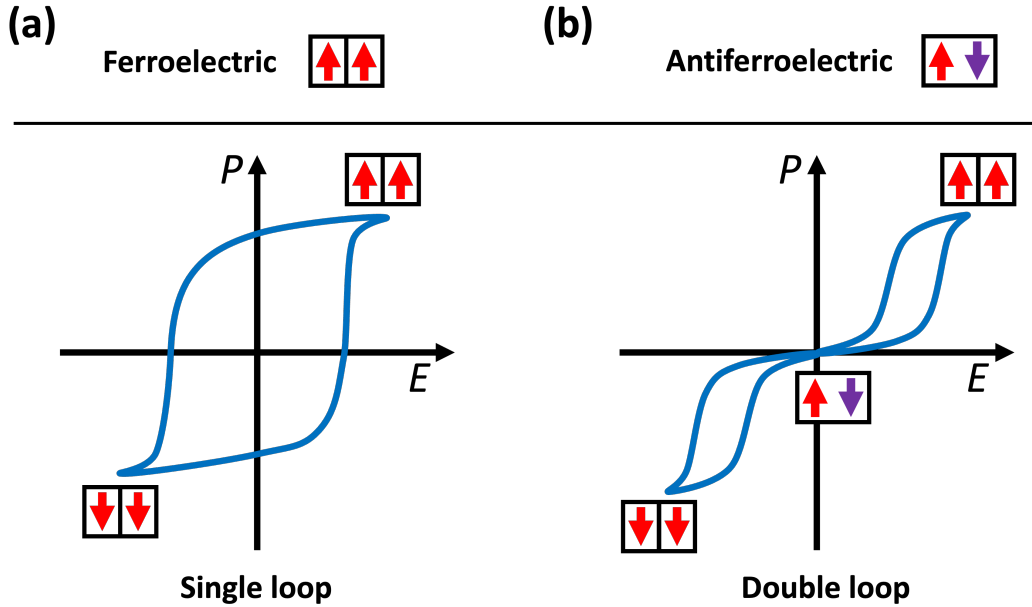

FIG. S1: Schematic of dipole alignments and P-E hysteresis loops of (a) ferroelectric, and (b) antiferroelectric materials. The arrows denote the electric dipoles and the black rectangle represents the unit cell.

SECTION S2. COMPUTATIONAL DETAILS

Monte-Carlo (MC) simulations are employed to study the behaviors of (001)-oriented $BiFeO_3$ (BFO) films at finite temperatures and under electric field, based on an effective Hamiltonian (H_{eff}) scheme. The Hamiltonian includes four types of degrees of freedom: 1) the local modes $\{u_i\}$ centered on the Bi sites, which are proportional to the local electric dipoles [1, 2]; 2) the homogeneous strain $\{\eta_H\}$ for the entire supercell and inhomogeneous strain $\{\eta_I\}$ for each unit cell [1, 2]; 3) the pseudovectors $\{\omega_i\}$ of oxygen octahedral tiltings [3]; and 4) the magnetic moments $\{m_i\}$ of the Fe ions. The subscript i labels unit cells in the simulated supercells.

The total energy can be expressed as a sum of two terms:

$$E_{tot} = E_{BFO}(\{u_i\}, \{\eta_H\}, \{\eta_I\}, \{\omega_i\}, \{m_i\}) + E_{depol}(\{u_i\}) , \qquad (1)$$

where E_{BFO} is the effective Hamiltonian of BFO that has been detailed in previous works [4–7]. E_{depol} represents the energy due to depolarizing field with $E_{depol} = \beta \sum_i \mathcal{E}_{depol} \cdot u_i$, where $\mathcal{E}_{depol}$ is the depolarizing field [8]. The coefficient β controls the screening condition of the depolarizing field [9], with $\beta = 1$ and $\beta = 0$ corresponding to ideal short-circuit (full screening) and open-circuit (no screening) electrical boundary conditions, respectively, while $0 < \beta < 1$ corresponds to cases of incomplete screening.

We simulate (001)-oriented BFO films using $12 \times 12 \times N_z$ supercells with periodic boundary conditions along the in-plane directions. N_z represents the number of 5-atom perovskite unit cells along the film's growth direction and ranges from 2 to 48. The simulations consider one vacuum and two substrate layers with zero values of local modes, octahedral tiltings, and magnetic moments. MC simulations were carried out using 40000 sweeps, which are sufficient to obtain converged results. Moreover, when an external electric field $\mathcal{E}$ is applied, an additional energy term with the form $-\sum_i p_i \cdot \mathcal{E}$ is incorporated, where the local electric dipoles p_i are computed from the local modes $\{u_i\}$ and Born effective charge. Note that the simulated electric field is known to be overestimated as explained by Landauer's paradox [10]. Numerically, a factor of 25 has been found for the *R3c* phase of BFO by comparing the coercive fields between MC simulation and experiment [11], and such scale factor has been considered in the present study.

SECTION S3. BULK VS. FILM STRUCTURES

In bulk BFO, the R phase is characterized by a large homogeneous polarization along the pseudocubic [111] direction with $P_x = P_y = P_z = 41$ μC/cm^2 [dashed lines in Fig. S2(a)] and antiphase octahedral tiltings with an $a^-a^-a^-$ pattern with an angle of 8.14 degrees [dashed lines in Fig. S2(b)]. The O phase features anti-parallel dipoles oriented along [110] and [$\bar{1}\bar{1}0$] directions in alternating layers along the z direction, resulting in zero net polarization [dashed lines in Fig. S2(c)]. This phase is further characterized by in-plane antiphase octahedral tiltings of 9.45 degrees and out-of-plane in-phase tiltings of 8.54 degrees (represented by a$^-$a$^-$c$^+$) [Fig. S2(d)]. In contrast, the T phase displays exclusively [001]-oriented polarization and an absence of octahedral rotation [Fig. S2(e) and (f)].

For a BFO film, under short-circuit condition, the structure differs from its bulk counterpart due to the surface effect. Taking a representative 6-layer film as an example, Fig. S2 shows the layer-by-layer polarization and octahedral tiltings of the R-like, O-like, and T-like phases, in comparison with the bulk R, O, and T phases. In the R-like phase, the
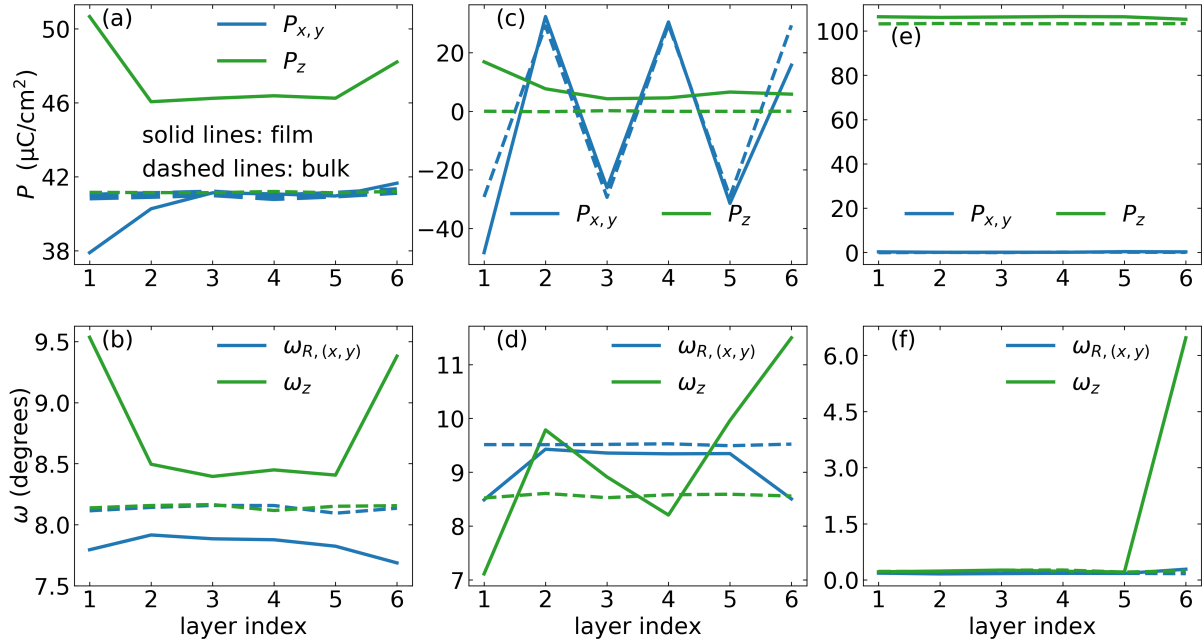

FIG. S2: Layer-by-layer decomposed polarization and oxygen octahedral tilting in a 6-layer BFO film predicted by Monte Carlo simulations at 10 K, compared with bulk BFO. Solid and dashed lines denote data from film and bulk, respectively. (a), (b) R-like and R phases. (c), (d) O-like and O phases. (e), (f) T-like and T phases.

polarization appears to be homogeneous in the middle layers, while the two surface layers show significant changes with apparently larger P_z than the interior. And in each layer, the out-of-plane component of the polarization is larger than the in-plane components [solid lines in Fig. S2(a)]. A similar inhomogeneity is found in octahedral tiltings. The out-of-plane antiphase octahedral tiltings increase by approximately 0.3 degrees and 2 degrees for the interior and surface layers, respectively, compared to their bulk counterparts. In contrast, the in-plane antiphase octahedral tiltings show a reduction relative to the bulk values [see Fig. S2(b)]. In the O-like phase, a key characteristic is the emergence of a notable out-of-plane polarization in thin films, which is further enhanced in the surface layers [Fig. S2(c)]. The in-plane component of the polarization is along the [110] and [$\bar{1}\bar{1}0$] directions in alternating layers along the z direction, while the magnitude of $P_{x,y}$ shows a clear variation at surface layers compared with the relative uniformity in interior regions [Fig. S2(c)]. Comparing T-like with T phase, the polarization direction and magnitude are very similar, while its surface layer undergoes substantial structural distortion with octahedral rotations over 6 degrees [Fig. S2(e) and (f)]. To characterize the structural deviations of film phases from their bulk counterparts, Table S1 summarizes key differences in the overall dipole (P), average anti-polar vector (X), anti-phase octahedral tilting (ω_R), and in-phase oxygen octahedral tilting (ω_M) patterns. In addition, the atomic structures are illustrated in Fig. S3.

TABLE S1: Overall characteristics of the bulk and film phases. P denotes the average polarization vector, X the average anti-polar vector, ω_R the average anti-phase octahedral tilting vector, and ω_M the average in-phase octahedral tilting vector. Superscript $'$ indicates that the corresponding magnitude in film differs from that in the bulk. The $\star$ marker in the T-like phases indicates that octahedral rotation occurs only in the surface layer [see Fig. S2(f)].

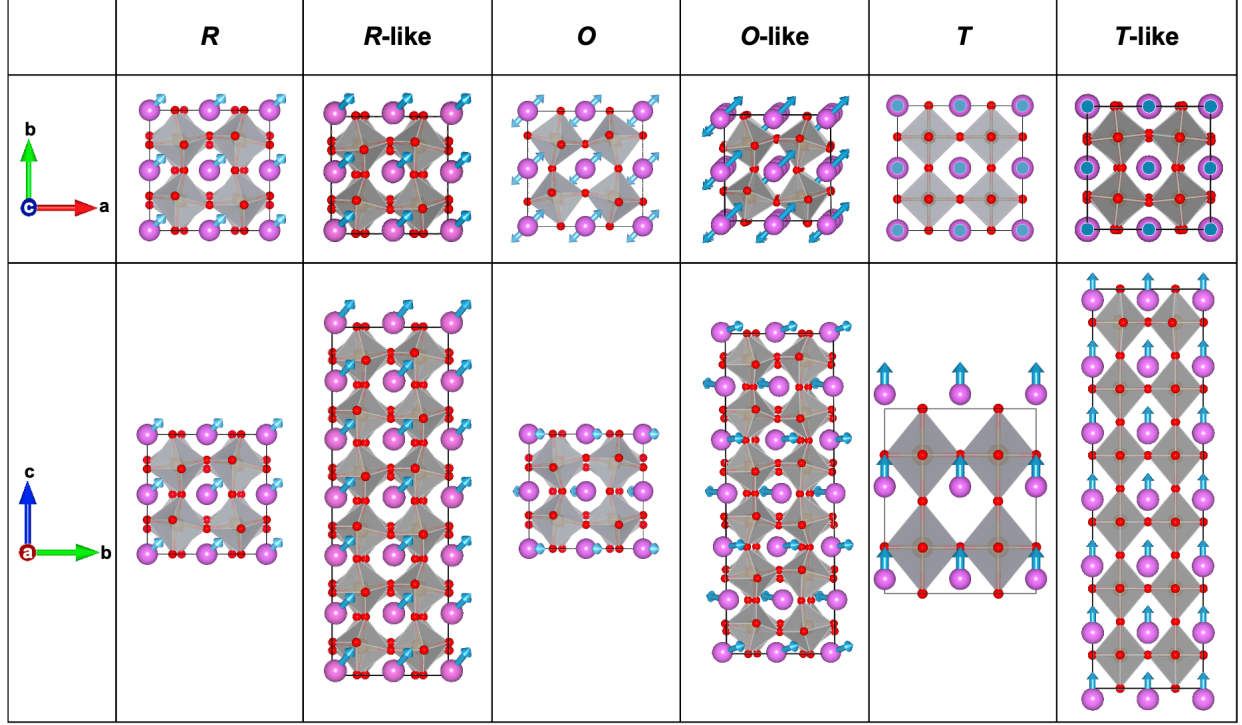| Phase | Bulk | | | Film | | |
	R	O	T	R-like	O-like	T-like
P	$[uuu]$	$[000]$	$[00u]$	$[u'u'v']$ $(u' < v')$	$[u'u'v']$ $(u' < v')$	$[00u']$
X	$[000]$	$[uu0]$	$[000]$	$[000]$	$[u'u'0]$	$[000]$
ω_R	$a^-a^-a^-$	$a^-a^-c^0$	$a^0a^0a^0$	$a'^-a'^-c'^-$	$a'^-a'^-c'^-$	$a^0a^0c^\star$
ω_M	$a^0a^0a^0$	$a^0a^0c^+$	$a^0a^0a^0$	$a^0a^0a^0$	$a^0a^0c'^+$	$a^0a^0c^\star$

FIG. S3: Comparison between bulk (R, O, and T) and film (R-like, O-like, and T-like) structures. Blue arrows indicate the dipole patterns, shown on the Bi ions. Film structures are illustrated for a thickness of 6 unit cells.

For each structure, changing the film thickness has a quantitative effect, as shown in Fig. S4. In the R-like phase, as thickness decreases, P_z increases while $P_{x,y}$ decreases, indicating that the polarization rotates towards the out-of-plane direction. Antiphase octahedral tiltings show a similar trend in this phase, i.e., $\omega_{R,z}$ increases and $\omega_{R,(x,y)}$ decreases. In the O-like phase, the polarization components are significantly enhanced as the film thickness is reduced, reaching an impressive 34 μC/cm^2 for out-of-plane polarization in the 2-unit-cell-thick film. In contrast, films thicker than 8 nm exhibit nearly zero polarization, closely resembling the O phase. And as the film thickness decreases, there is an increase in out-of-plane in-phase octahedral tiltings, whereas in-plane antiphase tiltings have a slight reduction. As for the T-like phase, the polarization remains nearly constant, while the octahedral rotation around the z axis emerges with pronounced thickness dependence. Note that the coexistence of $\omega_{R,z}$ and $\omega_{M,z}$ with identical magnitudes is in fact a result of the octahedral rotation only in the surface layer [see Fig. S2(f)].
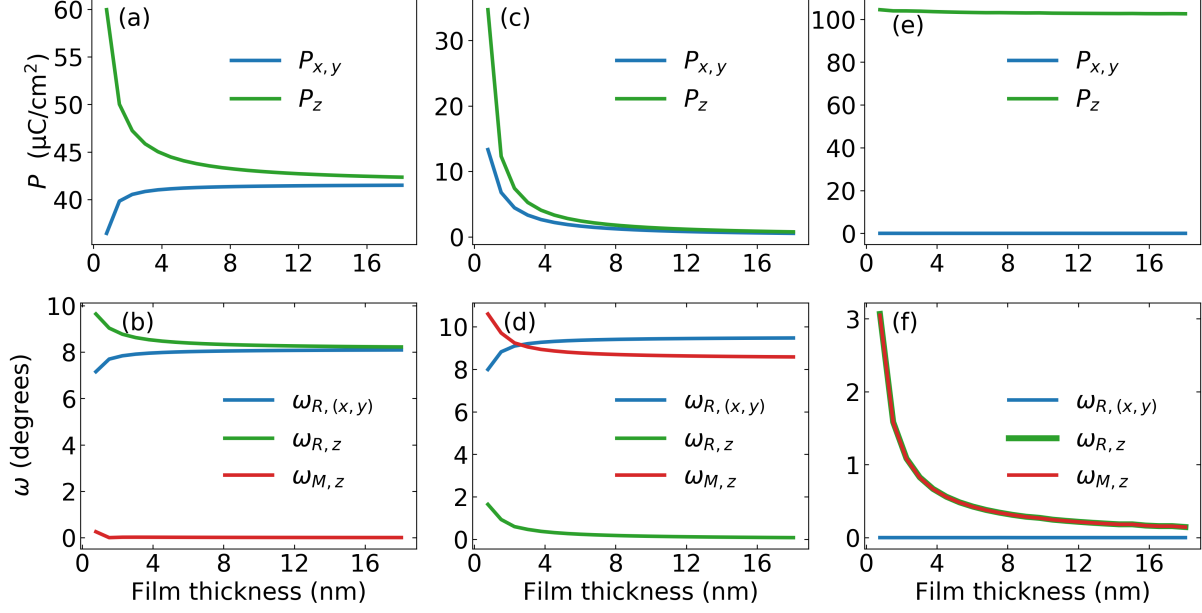
FIG. S4: Polarization and octahedral tilting as a function of BFO film thickness predicted by Monte Carlo simulations at 10 K. (a), (b) R-like phase. (c), (d) O-like phase. (e), (f) T-like phase.

SECTION S4. ELECTROSTATIC MODEL TO EXPLAIN THE POLARIZATION IN THE O-LIKE PHASE

To see the physical origin of the emergence of polarization in the O-like phase in BFO film from a different viewpoint, we also compute the thickness-dependent polarization according to the electrostatic model proposed in Ref. [12]. The total energy per unit area of the film can be expressed as a sum of three terms.

$$
\begin{aligned}
E_{\text{tot}} &= E_{\text{int}}d + E_{\text{es}} + E_{\text{scr}} \\
&= (aP_\xi^2 + bP_\xi^4)d + \frac{(P_{\text{layer}} - P_\xi - \sigma_{\text{scr}})^2}{2\epsilon_0\epsilon_{\text{r}}}d + \frac{\sigma_{scr}}{e}E_g
\end{aligned} \tag{2}
$$

In the first term, E_{int} is the internal energy per volume, which arises from the ferroelectric-like distortion P_ξ, and d is the film thickness. The second term describes the electrostatic energy from any unscreened polarization perpendicular to the slab surface, with P_{layer} being the polarization due to charged surface layers, σ_{scr} the magnitude of the screening charge per unit area on each surface, and ϵ_{r} the dielectric susceptibility. The third term is the screening energy when there are electron-hole pairs generated across the band gap E_g (see details in Ref. [12]).
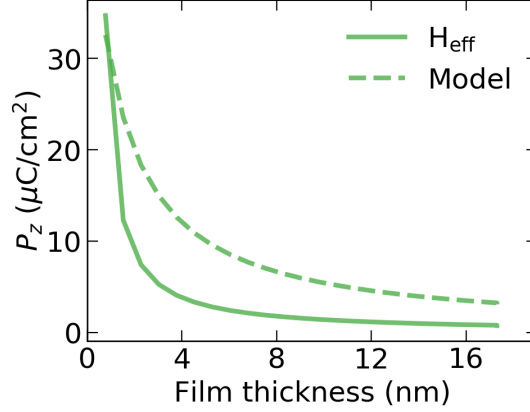
FIG. S5: Comparison of the out-of-plane polarization of the O-like phase as a function of BFO film thickness computed by effective Hamiltonian and the electrostatic model of Eq. (2) in the Supplemental Material.

To compute P_ξ for each thickness, we minimize the total energy with respect to σ_{scr} and P_ξ, and solve the equations as described in Ref. [12]. The quadratic and quartic coefficients in the Landau energy of E_{int} are computed by fitting the E vs. P_z curve with fixed $a^- a^- c^+$ oxygen octahedral tilting and G-type antiferromagnetization for the O phase, which yields $a = 0.929$ eV/(C^2/m^4) and $b = 0.814$ eV/(C^4/m^8). The experimental band gap of $E_g = 2.8$ eV of bulk BFO in Ref. [13] is adopted. The estimated variation of P_ξ as a function of film thickness based on the electrostatic model of Eq. (2) is shown as the dashed line in Fig. S5. We also depict P_z calculated with the effective Hamiltonian method (solid line), and these two approaches yield similar thickness dependence and magnitudes. Note that ferroelectric-like P_ξ of the electrostatic model is the same as the z-component of polarization in our effective Hamiltonian.

SECTION S5. SIMPLE MODEL TO EXPLAIN THE FE-TO-AFE SIZE EFFECT

The transition from the R-like to O-like phase in BFO film with decreasing thickness is primarily governed by a shift in the balance between long-range (LR) and short-range (SR) dipole-dipole interactions.

The LR dipole-dipole interaction is derived from the Coulomb interaction between dipoles, modulated by the dielectric screening. According to ref. [1], this energy can be expressed as
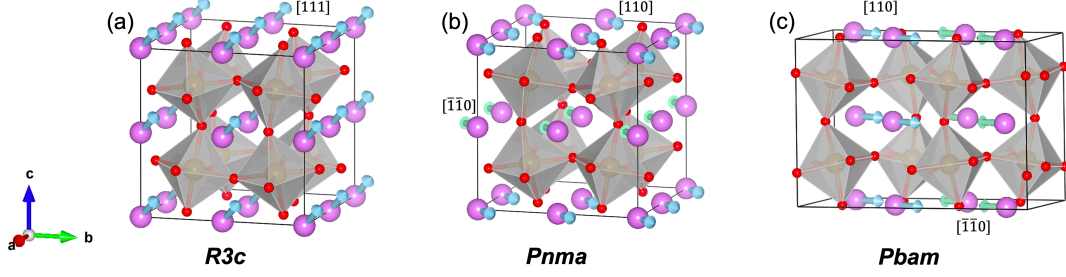
FIG. S6: Structures of the (a) *R3c*, (b) *Pnma*, and (c) *Pbam* phases.

$$E^{\text{dpl}}(\{\mathbf{u}\}) = \frac{Z^{*2}}{\epsilon_\infty} \sum_{i<j} \frac{\mathbf{u}_i \cdot \mathbf{u}_j - 3(\hat{\mathbf{R}}_{ij} \cdot \mathbf{u}_i)(\hat{\mathbf{R}}_{ij} \cdot \mathbf{u}_j)}{R_{ij}^3} \ , \tag{3}$$

where $\mathbf{u}_i$ is the soft mode at site i, Z^* is the Born effective charge according to the eigenvector of soft mode, ϵ_∞ is the optical dielectric constant, and $\mathbf{R}_i$ is the lattice vector with $\mathbf{R}_{ij} = \mathbf{R}_i - \mathbf{R}_j$ and $\hat{\mathbf{R}}_{ij} = \mathbf{R}_{ij}/|\mathbf{R}_{ij}|$.

In practice, E^{dpl} is evaluated using an Ewald construction, and it can be written as

$$E^{\text{dpl}} = \sum_{ij,\alpha\beta} Q_{ij,\alpha\beta} u_{i,\alpha} u_{j,\beta} \ , \tag{4}$$

with

$$Q_{ij,\alpha\beta} = \frac{2Z^{*2}}{\epsilon_\infty} \left[\frac{\pi}{\Omega_c} \sum_{\mathbf{G}\neq 0} \frac{1}{|\mathbf{G}|^2} \exp\left(-\frac{|\mathbf{G}|^2}{4\lambda^2}\right) \cos(\mathbf{G} \cdot \mathbf{R}_{ij}) G_\alpha G_\beta - \frac{\lambda^3}{3\sqrt{\pi}} \delta_{\alpha\beta} \delta_{ij} \right] \ , \tag{5}$$

where Ω_c is the unit cell volume and $\mathbf{G}$ is the reciprocal lattice vector.

On the other hand, the SR energy contribution is due to the short-range interactions between neighboring local modes, with LR dipole-dipole interactions excluded. SR dipole-dipole interactions do not arise from classical long-range electrostatics, but rather from local chemical bonding and electronic structure effects. This contribution stems from electronic hybridization effects, i.e., displacements of ions in neighboring cells can enhance or suppress the hybridization, leading to energetic coupling, as well as short-range Pauli repulsion and bonding. When local modes in adjacent cells distort the local structure, they alter bond lengths and angles, modifying ionic and covalent bonding. The SR interaction energy decays rapidly with distance and can be written in the following form.

$$E^{\text{short}} = \frac{1}{2} \sum_{i\neq j} \sum_{\alpha\beta} J_{ij,\alpha\beta} u_{i\alpha} u_{j\beta}. \tag{6}$$

9

Here, $J_{ij,\alpha\beta}$ is the coupling matrix. For the first-nearest-neighbor SR interactions that are considered in our model [see Eq. (2) of the manuscript], $J_{ij\alpha\beta}$ equals to $(j_1 + (j_2 - j_1)|\hat{\mathbf{R}}_{ij,\alpha}|)\delta_{\alpha\beta}$, with $\delta_{\alpha\beta}$ being the Kronecker symbol, the j_1 and j_2 pairs illustrated in the inset of Fig. 2 and their values listed in Table I of the manuscript.

For simplicity, we only consider the dominant first-nearest-neighbor (1NN) short-range interactions, i.e., the j_1 and j_2 terms as illustrated in Fig. 2 of the main text. j_1 represents the "π"-like interactions and j_2 represents the repulsion between "head-to-tail" dipoles.

FIG. S7: Illustration of short-range interactions between first-nearest-neighbor dipoles in the FE and AFE phases of bulk BFO and PZO. Arrows denote the x-, y-, and z-components of the local dipoles.

In bulk BFO, to understand why the j_1 terms only contribute in the R phase but not in the O phase, we show the dipole patterns of these two structures in Fig. S6 and the

pair of components of the dipoles that belong to the j_1 terms in Fig. S7. The R phase is characterized by dipoles uniformly oriented along the pseudocubic [111] direction; hence, all the x-, y-, and z-components of the 1NN pairs can contribute. But in the O phase, the dipoles are aligned along the [110] and [$\bar{1}\bar{1}0$] directions alternately in the (001) layers, such that the j_1 contributions from the intra-layer pairs cancel with those from the inter-layer pairs. On the other hand, j_2 pairs can contribute in both the FE R and the AFE O phases, as illustrate in Fig. S7.
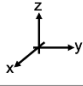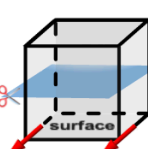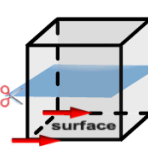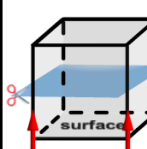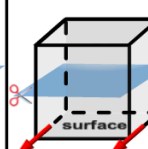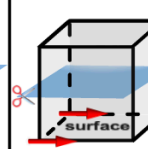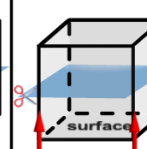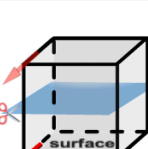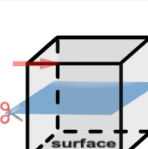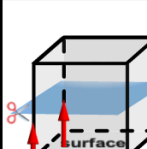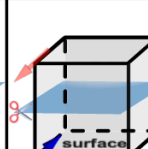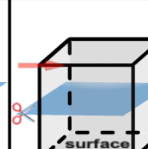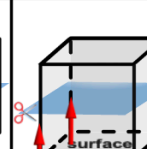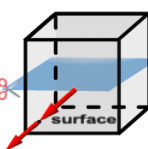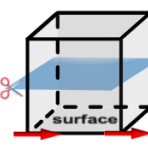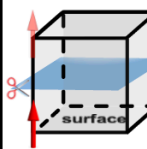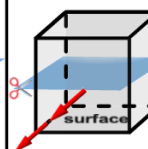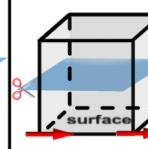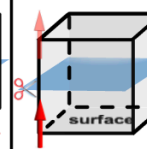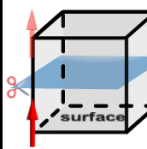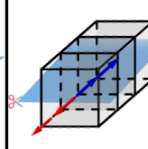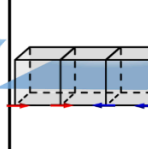
FIG. S8: Illustration of short-range interactions between first-nearest-neighbor dipoles in the surface layer of the FE and AFE-like phases of BFO and PZO films. Arrows denote the x-, y-, and z-components of the local dipoles. The blue horizontal plane indicates termination at the surface. Lightly colored arrows denote components of the missing dipoles beyond the surface layer.

11

In the film case, as shown in Fig. S8, the 1NN interactions for the R-like phase remain similar to that of the bulk except the missing inter-layer pairs at the two surfaces. While for the O-like phase, the main difference compared with the bulk is in the surface layers, where the anti-aligned inter-layer j_1 pairs are now absent. Also considering the emergence of out-of-plane components of the dipoles in the O-like phase, the 1NN contributions from the surface layers become similar in the R-like and O-like phases.

We also list the 1NN contributions of PZO for comparison, which has a tetragonal ferroelectric phase in PZO ultrathin film according to Ref. [14], and has the $Pbam$ structure as its antiferroelctric phase. The $Pbam$ phase is characterized by intra-layer "↑↑↓↓" dipole arrangement along the [110] direction [see Fig. S6(c)], which is associated with reciprocal space point $\Sigma = \frac{2\pi}{a}(0.25, 0.25, 0)$. Another major difference between PZO and BFO is that the interaction strength of the j_1 term in PZO can be neglected compared with j_2. By only considering j_2 interactions in PZO, there is zero contribution in its AFE phase, due to equal number of parallel and anti-parallel intra-layer pairs.

SECTION S6. P-E LOOPS WITH VARIOUS SCREENING AND TEMPERATURE CONDITIONS

As demonstrated in the main text, the ground state of an ultrathin BFO film (below ∼2 nm or 6 unit cells) under short circuit condition ($\beta = 1$) is the O-like phase, which possesses an out-of-plane polarization. To check if P_z in the 2-u.c. or 4-u.c. film can be switched by an electric field, we start from the O-like phase with positive P_z and apply a field along the [00$\bar{1}$] direction at 10 K. As shown in Fig. S9(a) and S9(b), P_z decreases continuously under the negative field until a phase transition to the T-like phase occurs. Reversing the field direction yields a single loop involving only the T-like phase [Fig. S9(c)]. For films thicker than 2 nm, the ground is the R-like phase, and a single loop involving the R-like phase can be obtained [see Fig. S9(d)].
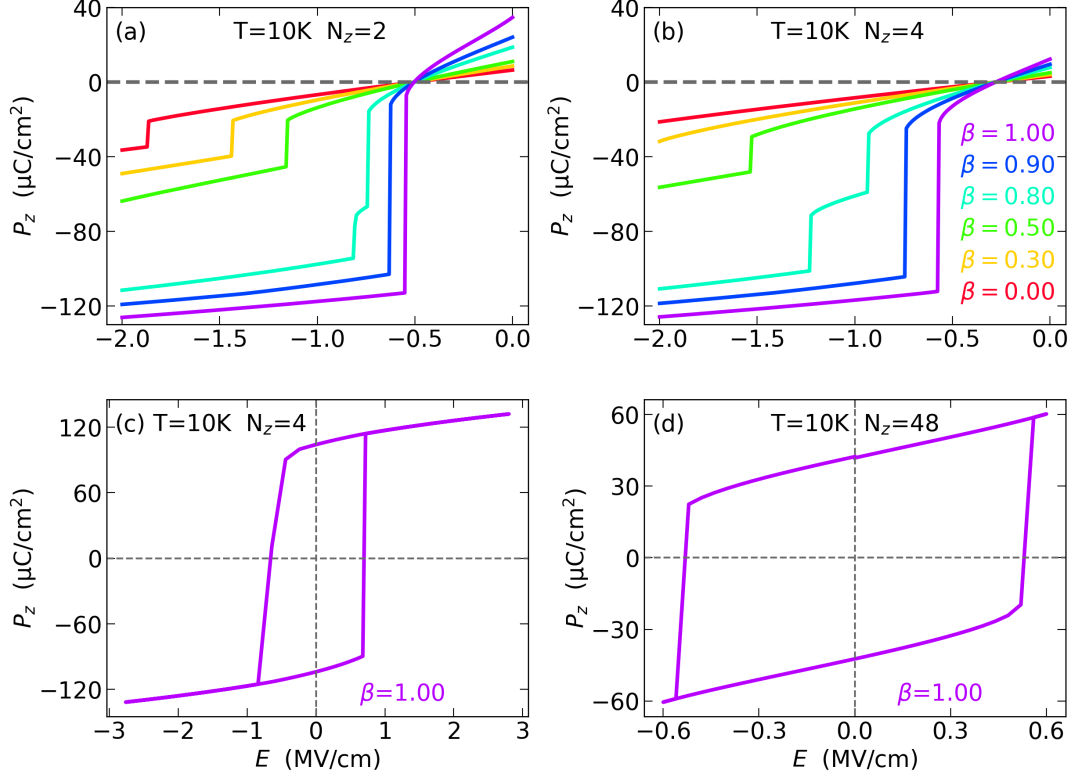
FIG. S9: Polarization switching behaviors of a BFO film under $[00\bar{1}]$-electric field at 10 K. The z-component of polarization as a function of electric field, starting from the O-like phase of (a) 2-layer film, and (b) 4-layer film with various electrostatic screening conditions. The hysteresis loop of (c) 4-layer film, and (d) 48-layer film under short-circuit conditions.
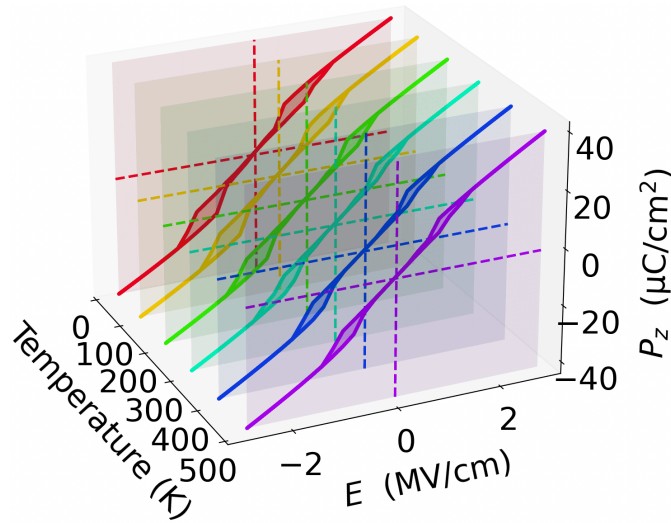

FIG. S10: P-E hysteresis loops for a 12-unit-cell-thick film under open-circuit conditions at various temperatures from 10 K to 500 K.

We also study the effect of surface screening condition on the switching behaviors. For films with 2 or 4 u.c. thickness, reducing the β value (less screening and larger depolarizing field) further stabilizes the O-like phase over the R-like phase [Fig. S9(a) and S9(b)]. Meanwhile, the out-of-plane polarization gradually diminishes due to the depolarizing field. Therefore, the O-like can sustain under larger negative field, as the screening is reduced. Nevertheless, the depolarizing field destabilizes more of the T-like phase as it has a very large polarization, and a transition from the O-like to the R-like phase can occur with β smaller than 0.8 [Fig. S9(a) and S9(b)].

Double hysteresis loops can be realized only in partially screened (including open-circuit) conditions, as shown in Fig. 3(b) of the main text. The effect of temperature on the double loop is quantitative, i.e., the loop size slightly shrinks as temperature increases, as shown in Fig. S10.

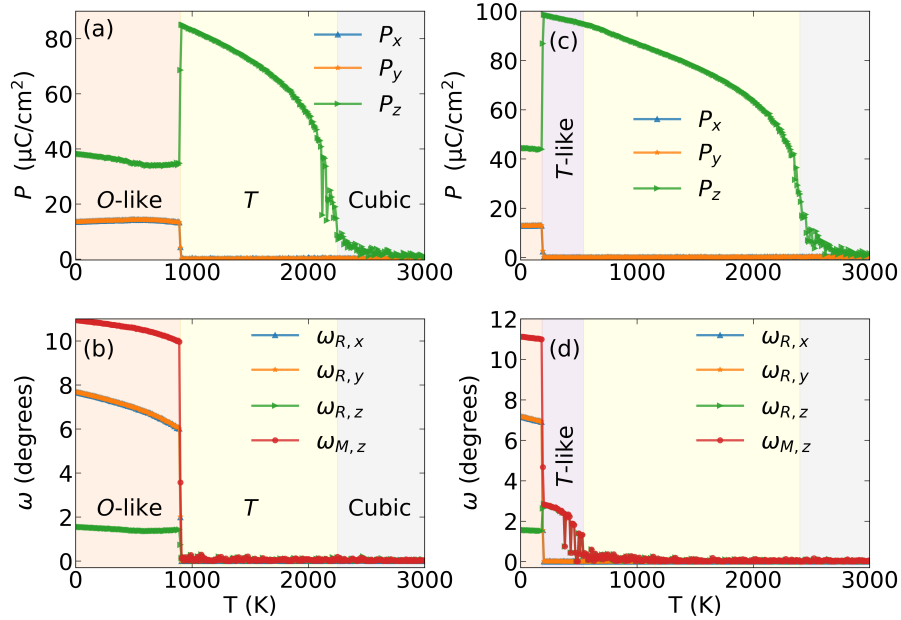## SECTION S7. STRAIN AND SURFACE SCREENING EFFECTS ON THERMAL STABILITY

FIG. S11: Temperature dependence of polarization and octahedral tilting in a 2-unit-cell-thick BFO film under compressive strain and short-circuit boundary conditions. (a), (b) -2% biaxial strain. (c), (d) -3% biaxial strain.
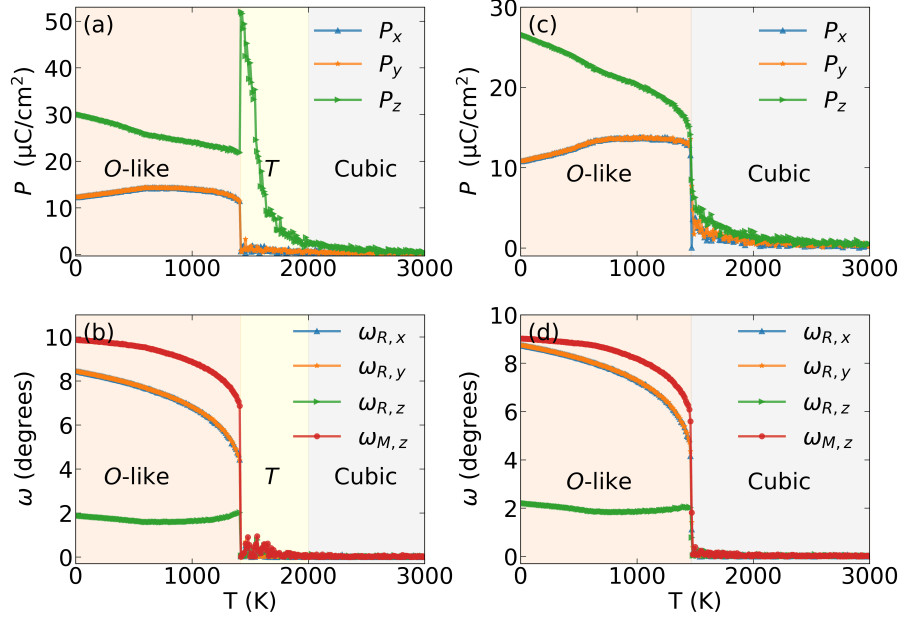
FIG. S12: Temperature dependence of polarization and octahedral tilting in a 2-unit-cell-thick BFO film under tensile strain and short-circuit boundary conditions. (a), (b) 0.5% biaxial strain. (c), (d) 2% biaxial strain.

In Fig. 4 of the main text, we show the prediction that the T phase can be stabilized between 1000 and 2000 K. Here, we further demonstrate that the T phase can be achieved at a lower temperature if compressive biaxial strain is applied. Figure S11 depicts the components of polarization, antiphase and inphase octahedral tiltings as a function of temperature for a -2% biaxial strain. The T phase becomes the ground state at ~ 900 K. For a slightly larger strain of -3%, an O-like to T-like transition can occur at a temperature as low as 185 K [see Fig. S11(c)], and the T-like phase transforms into the T phase at ~ 500 K, characterized by a smooth change in the polarization and diminishing octahedral rotation around the z axis. With further increase of the compressive strain, the T-like phase becomes the ground state even at very low temperature, as it is favored by the compressive strain. Conversely, the O-like phase is favored by tensile strain, which remains stable up to ~ 1400 K at 0.5 % strain [see Fig. S12(c)]. Upon further increasing the tensile strain, only the O-like phase is further stabilized, while the T-like phase vanishes. These behaviors are expected, since the structure with large out-of-plane polarization (or in-plane dipoles) is energetically more stable under compressive (or tensile) strain. In particular, a compressive strain larger than $\sim -3\%$ can suppress the O-like phase, and the intermediate T phase disappears for tensile

strain larger than ~2%.

On the other hand, reducing surface charge screening (decreasing β value or increasing depolarization field) has an effect of reducing the out-of-plane polarization, hence it favors the O-like phase. As shown in Fig. S13, the transition temperature from O-like to T becomes higher under a smaller β, i.e., 1025 K at $\beta = 1.00$ to 1240 K at $\beta = 0.98$. Further reduction of β can suppress the occurrence of the intermediate T phase.
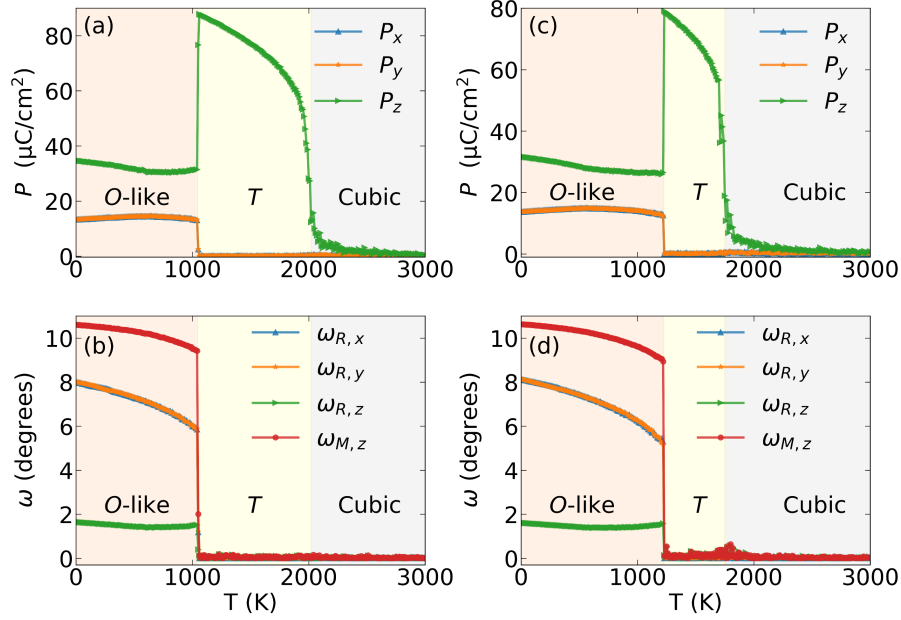

FIG. S13: Temperature dependence of polarization and octahedral tilting in a 2-unit-cell-thick BiFeO$_3$ film under various electrical boundary conditions. (a) and (b) β=1.00, (c) and (d) β=0.98.

---

* Email address: smantri@uark.edu

† Email address: binxu19@suda.edu.cn

[1] W. Zhong, D. Vanderbilt, and K. Rabe, Phys. Rev. B **52**, 6301 (1995).

[2] W. Zhong, D. Vanderbilt, and K. Rabe, Phys. Rev. Lett. **73**, 1861 (1994).

[3] I. A. Kornev, L. Bellaiche, P.-E. Janolin, B. Dkhil, and E. Suard, Phys. Rev. Lett. **97**, 157601 (2006).

[4] S. Prosandeev, D. Wang, W. Ren, J. Íñiguez, and L. Bellaiche, Adv. Funct. Mater. **23**, 234 (2013).

[5] D. Albrecht, S. Lisenkov, W. Ren, D. Rahmedov, I. A. Kornev, and L. Bellaiche, Phys. Rev. B **81**, 140401 (2010).

[6] I. A. Kornev, S. Lisenkov, R. Haumont, B. Dkhil, and L. Bellaiche, Phys. Rev. Lett. **99**, 227602 (2007).

[7] S. Lisenkov, I. A. Kornev, and L. Bellaiche, Phys. Rev. B **79**, 012101 (2009).

[8] I. Ponomareva, I. Naumov, I. Kornev, H. Fu, and L. Bellaiche, Phys. Rev. B **72**, 140102 (2005).

[9] S. Mantri, S. Prokhorenko, Y. Nahas, and L. Bellaiche, Phys. Rev. Mater. **8**, 104406 (2024).

[10] R. Landauer, J. Appl. Phys. **28**, 227 (1957).

[11] C. Daumont, W. Ren, I. Infante, S. Lisenkov, J. Allibe, C. Carrétéro, S. Fusil, E. Jacquet, T. Bouvet, F. Bouamrane, et al., J. Phys. Condens. Matter **24**, 162202 (2012).

[12] C. Gattinoni and N. A. Spaldin, Phys. Rev. Res. **4**, L032020 (2022).

[13] S. Clark and J. Robertson, Appl. Phys. Lett. **90**, 132903 (2007).

[14] B. Mani, C.-M. Chang, S. Lisenkov, and I. Ponomareva, Phys. Rev. Lett. **115**, 097601 (2015).